

Adenine-Derived Nitrogen-doped Porous Carbon for High-Performance Supercapacitor Electrodes and Carbon Dioxide Capture

Xia Jiang^{1,2,3*}

¹ Weihai Ocean Vocational College, Weihai, Shandong 264300, P.R. China.

² College of Chemistry and Molecular Engineering, Qingdao University of Science and Technology, Qingdao, Shandong 266042, P.R. China.

³ Shandong Dyne Marine Biopharmaceutical Co., Ltd., Weihai, Shandong 264300, P.R. China.

*E-mail: jiangxiazzu@163.com

Received: 2 July 2022/ Accepted: 5 August 2022/ Published: 10 September 2022

We present a sustainable pathway for the synthesis of nitrogen-doped porous carbon (NPC) via hydrothermal carbonization coupled with KOH activation using biobased adenine and glucose as nitrogen sources and carbon sources, respectively. The porosity and chemical properties of NPC can be tailored by the activation temperature and the amount of activation agent. The as-synthesized NPC possesses abundant ultramicropores (approximately 0.7 nm), an ultrahigh surface area (up to 3273 m² g⁻¹) and a nitrogen content of 7.03 wt%. As a supercapacitor electrode, NPC exhibits a high specific capacitance of 333 F g⁻¹ at 0.5 A g⁻¹ in 6.0 M KOH and an excellent cycle stability (retaining 92.7% specific capacitance after 5000 cycles). Moreover, NPC shows high CO₂ uptake of 6.7 mmol g⁻¹ (at 0 °C) and 4.4 mmol g⁻¹ (at 25 °C) at 1 bar, as well as excellent CO₂ selectivity against N₂. These results indicate that the obtained NPC is a promising electrode material for supercapacitors and solid adsorbents for CO₂ capture.

Keywords: Adenine; Nitrogen-doped; Porous carbon; Supercapacitors; CO₂ capture

1. INTRODUCTION

Porous carbon is an ideal candidate for energy and environmental applications, including adsorption, catalysis support, and energy storage, owing to its large surface area, controllable pore size distribution and chemical inertness [1-4]. To date, various carbon materials with well-defined porosities have been prepared via activation and template methods [5-7]. However, these porous carbon materials suffer from hydrophobic surfaces and limited specific active sites. Extensive investigations have demonstrated that the incorporation of nitrogen into carbon frameworks significantly improves the conductivity, surface polarity, and electronic structure of carbon [8-10]. Generally, high porosity not

only provides a large reservoir for charge accommodation or CO₂ storage but also offers accessible channels for ion or gas transfer. On the other hand, surface nitrogen functionality can generate pseudocapacitance derived from redox reactions between nitrogen groups and electrolytes, as well as enhancing CO₂ uptake because of the strong interaction between basic nitrogen species and CO₂ molecules [11-13]. As such, nitrogen-doped carbon materials with high surface area and nitrogen content have been increasingly investigated.

Pyrolysis/carbonization of nitrogen-containing precursors (e.g., synthetic polymers and organic molecules) is a common approach to synthesize nitrogen-doped porous carbon [14,15]. However, these nitrogen-containing precursors suffer from toxicity or relatively high cost. Recently, biobased nitrogen-doped porous carbon has received considerable attention because these biobased precursors are relatively cheap, available and sustainable. They include gelatin [16], glucosamine [12,17], chitosan [12], glycine [18], and amino acids [19]. Hydrothermal carbonization (HTC) has suggested to be an effective strategy for the conversion of biobased precursors into carbonaceous compounds (so-called hydrochar), followed by carbonization/activation to produce nitrogen-doped porous carbon. Titirici and coworkers employed glucosamine as a precursor for the synthesis of nitrogen-doped porous carbon via HTC and KOH activation¹², which exhibited high capacitive performance. The results demonstrated that it is a feasible route to fabricate nitrogen-doped porous carbon using biobased compounds as precursors via HTC and KOH activation. However, the abovementioned nitrogen-containing sources possess a relatively low nitrogen content (< 20 wt%), resulting in a small fraction of nitrogen species doping on carbon materials. Interestingly, sustainable biobased nucleobases (adenine, guanine, thymine, cytosine, uracil) with high nitrogen content (> 20 wt%) are promising nitrogen sources for the fabrication of nitrogen-doped carbon materials.

For the first time, in this work we employ adenine with a high nitrogen content (ca. 52 wt%) and glucose as precursors to synthesize nitrogen-doped porous carbon (NPC) via hydrothermal carbonization and KOH activation. The textural and chemical properties (e.g., surface area, pore size distribution and surface functionality) of NPC are investigated as a function of the amount of activated agent or activation temperature. The as-synthesized carbon materials possess well-developed ultramicropores (~0.7 nm), a very large surface area of 3273 m² g⁻¹ and a high nitrogen content (7.03 wt%). As supercapacitor electrodes, the carbon materials deliver a high specific capacitance of 333 F g⁻¹ at 0.5 A g⁻¹ in 6.0 M KOH with excellent cycle stability (retaining 92.7% of the specific capacitance after 5000 cycles). Moreover, these carbon materials also exhibit a high CO₂ uptake of 4.4 mmol g⁻¹ (25 °C) and excellent CO₂ selectivity against N₂ under ambient conditions.

2. EXPERIMENTAL CONDITIONS

2.1 Synthesis of nitrogen-doped porous carbon

For a typical procedure, 1 g of adenine and 2 g of glucose were dispersed in 30 mL distilled water. The solution was sealed in a TeflonTM-lined stainless autoclave and heated at 180 °C for 6 h. Then, the brown/black powder (the so-called hydrochar) was collected by filtration and washed with abundant

distilled water for drying at 105 °C. Next, the hydrochar was completely mixed with KOH at a KOH/hydrochar ratio of 1 or 2 for carbonization/activation at the desired temperatures (600, 700, and 800 °C) for 2 h with a heating rate of 3 °C min⁻¹ under argon. After that, the activated samples were washed several times with 10 wt% HCl to remove inorganic salts and were further rinsed with abundant distilled water until reaching neutral pH. After drying, the obtained carbon samples were assigned as NPC-x-y, where NPC stands for nitrogen-doped porous carbon, x is the weight ratio of hydrochar/KOH and y is the activation temperature.

2.2 Characterization

A field-emission scanning electron microscope (FESEM) equipped with an energy dispersive X-ray spectrometer (EDX) was used to observe the surface morphology and components of the carbon materials. High-resolution transmission electron microscopy (HRTEM) was performed at 200 kV to characterize the microstructure of the carbon materials. The structure of the carbon materials was investigated by X-ray diffraction (XRD, Bruker D8) with Cu radiation at 40 mA and 40 kV and Raman spectroscopy (Renishaw InVia) under 514 nm laser excitation. The porosity of the carbon was determined by nitrogen sorption at 77 K using an ASAP 2020 sorptometer (Micromeritics). The surface area (S_{BET}) was evaluated using the Brunauer-Emmett-Teller (BET) method at a relative pressure (P/P_0) of 0.05-0.2. The total pore volume (V_t) was calculated from the nitrogen uptake at a P/P_0 of ca. 0.99. The micropore surface area and volume were determined via t -plot analysis. Pore size distribution (PSD) was assessed using a nonlocal density functional theory (NLDFT) model. Elemental analysis was performed to analyze the material components on a Vario III elemental analyzer. X-ray photoelectron spectroscopy (XPS) was utilized to characterize the surface groups, taken from an ESCALAB 250Xi using standard Al K α radiation (1486.6 eV) working at 278 W.

2.3 Electrochemical measurements

All electrochemical tests were performed in 6.0 M KOH using a three-electrode system. We fabricated working electrodes by pressing a slurry of NPC (80 wt%), polytetrafluoroethylene (10 wt%) and carbon black (10 wt%) onto the Ni foam. The working electrode was dried at 100 °C under vacuum and then soaked in solution for 24 h before the electrochemical tests. A Pt plate and Hg/HgO electrode served as the counter electrode and reference electrode, respectively. We measured cyclic voltammetry (CV) and electrochemical impedance spectroscopy (EIS) on a Zahner IM6e electrochemical workstation to investigate the electrochemical performance. The CV curves were obtained in the range of -1 and 0 V, and the EIS measurements were carried out between 10 mHz and 100 kHz with an AC amplitude of 5 mV. The galvanostatic charge/discharge (GCD) tests were conducted on a CHI 660E electrochemical workstation between -1 and 0 V. The specific capacitance, C_g (F g⁻¹), was calculated using the following equation:

$$C_g = I\Delta t/m\Delta V \quad 1$$

in which I (A) is the discharge current, Δt (s) is the discharge time, m (g) is the active mass of the working electrode, and ΔV (V) is the potential window.

2.4 CO₂ uptake

The carbon dioxide isotherms were carried out on an ASAP 2020 under a pressure range of 0-1 bar at 0 and 25 °C. The temperature was controlled by a circulating bath. Highly purified carbon dioxide and nitrogen (99.999%) were used as adsorbates for all experiments. Before the adsorption analysis, the samples were degassed at 200 °C for 12 h.

The enthalpy of CO₂ adsorption for nitrogen-doped porous carbon was calculated from the Clausius-Clapeyron equation:

$$\ln\left(\frac{P_1}{P_2}\right) = \Delta H_{ads} \times \frac{T_2 - T_1}{R \times T_1 \times T_2} \quad 2$$

(T_i = temperature for isotherm i ; P_i = pressure for isotherm i ; $R = 8.314 \text{ J K}^{-1} \text{ mol}^{-1}$)

The pressure as a function of the amount of CO₂ adsorbed was determined using the Langmuir-Freundlich fit for the isotherms:

$$\frac{Q}{Q_m} = \frac{B \times P^{(1/t)}}{1 + B \times P^{(1/t)}} \quad 3$$

(Q = moles adsorbed; Q_m = moles adsorbed at saturation; P = pressure; B and t = constants)

Equation 3 can be rearranged to Equation 4. Finally, the isosteric heat of adsorption can be obtained by adding P into Equation 2.

$$P = \left(\frac{Q}{B(Q_m - Q)}\right)^t \quad 4$$

The experimental adsorption isotherms were first fitted using the single-site Langmuir model:

$$q_i = q_{i,sat} \frac{b_i p_i}{1 + b_i p_i} \quad 5$$

where b_i = Langmuir constant, Pa^{-1} ; p_i = bulk gas phase pressure of species i , Pa; q_i = molar loading of species i , mmol g^{-1} ; and $q_{i,sat}$ = saturation capacity of species i , mmol g^{-1} .

The fitted parameters obtained from the single-site Langmuir model and were used for the calculation of the ideal adsorption solution theory (IAST) selectivity.

According to the IAST proposed by Myers and Prausnitz, 1 the adsorption selectivity, S_{ads} , for binary mixtures of 1 and 2 is defined as:

$$S_{ads} = \frac{q_1/q_2}{p_1/p_2} \quad 6$$

In this study, selectivity calculations were carried out for CO₂/N₂ binary mixtures with N₂ molar fractions ranging from 70% to 100%, which is the typical composition range of flue gas.

3. RESULTS AND DISCUSSION

The schematic preparation processes for NPCs are shown in Figure 1.



Figure 1. The schematic synthesis of nitrogen-doped porous carbon

The morphology and microstructure of nitrogen-doped porous carbon were investigated using electron microscopy technologies. The FESEM image of the surface morphology of the as-synthesized hydrochar exhibits spherical particles with uniform size and smooth surface (Figure 2(a)). This spherical morphology provides a large interfacial area to react with KOH, which can develop a well-developed porous structure for carbon materials. After KOH activation, the resulting carbon materials show a different morphology. The representative FESEM image (Figure 2(b)) of NPC-1-600 displays the presence of holes with a three-dimensional framework in carbon materials. However, NPC-2-800 (Figure 2(c)) prepared with the severest activation exhibits smooth grooves and sharp edges due to the strong reaction between KOH and the precursors. Obviously, the activation conditions significantly affect the porosity and morphology of the carbon thus obtained, indicating that the porous structure can be tailored by chemical activation conditions. As illustrated by the HRTEM images, NPC-2-800 (Figure 2(d)) exhibits a uniform and large disordered microstructure with a large fraction of microporous structures and a few narrow mesoporous structures. This structure of nitrogen-doped carbon is of great importance for supercapacitors and CO₂ capture due to the abundant active sites and narrow pores.

The typical XRD patterns and Raman spectra of the as-synthesized NPC are displayed in Figure 3. All samples show two broad diffraction peaks distributed at ca. 25° and 43° corresponding to the (002) and (100) planes of graphitic carbon [20], respectively, which indicates the amorphous characteristic of these carbon materials. As the activation degree increases, the diffraction peaks of NPC gradually become lower and broader due to the breakdown of the graphitic structure caused by the intercalation of the potassium compounds into the carbon matrix during the carbonization/activation processes. Furthermore, we performed Raman spectroscopy to explore the graphitic structure of NPC shown in Figure 4(b), in which two typical peaks at 1334 cm⁻¹ (D band) and 1590 cm⁻¹ (G band) are observed. The former is associated with the defective and disordered structure of carbon materials, which benefits charge storage, and the latter is attributed to graphitic carbon with in-plane vibrations of the sp² electronic configuration, which can improve the electrical conductivity [21,22].

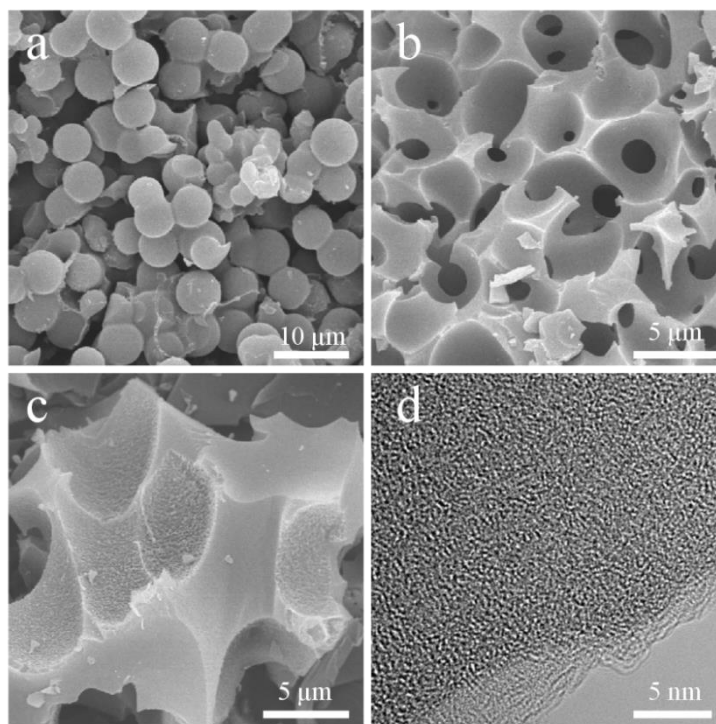


Figure 2. SEM images of hydrochar materials (a), NPC-1-600 (b) and NPC-2-800 (c), and HRTEM image of NPC-2-800 (d)

The intensity ratio of the D band to the G band (I_D/I_G) can roughly reflect the graphitization degree of carbon materials. As seen in the spectra, the I_D/I_G of NPC-1-600 is approximately 1.02, and the I_D/I_G has a slight increase with increasing activation degree, which indicates the formation of tiny long-range graphitic carbon with abundant structural defects and disordered structures of carbon materials, corresponding to the XRD results.

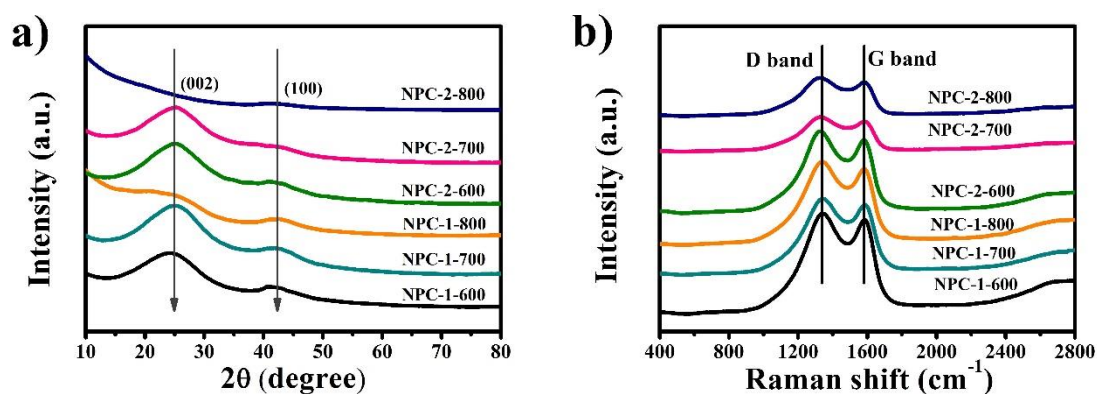


Figure 3. XRD patterns (a) and Raman spectra (b) of nitrogen-doped porous carbon

The porosity properties of the NPC were investigated by the analysis of nitrogen sorption isotherms displayed in Figure 4. Figure 4(a) shows that all NPC samples have a steep rise in N_2 uptake at low P/P_0 (< 0.1), after which they nearly maintain a plateau, which is the typical type-I isotherm, indicating the microporous characteristic of NPC. Importantly, all NPC materials show high N_2 uptake

at very low P/P_0 (<0.01), which is ascribed to the ultramicropores (< 1 nm). Additionally, the N_2 uptake of NPC at low P/P_0 is highly relative to the activation conditions, and the carbon materials prepared from a higher weight ratio of KOH/hydrochar or activation temperature possess higher N_2 uptake, suggesting the formation of more porous structures. On the other hand, the carbon materials prepared with a higher degree of activation have a broader isotherm knee, indicating the enlargement of pores. This is because the decomposition of K_2CO_3 at higher activation temperatures (> 700 °C) generates more CO_2 , leading to higher gasification [23]. In Figure 4(b), the pore size distribution curves of carbon materials indicate that NPC materials prepared with mild activation (KOH/hydrochar ratio of 1) mainly consist of micropores, especially ultramicropores (< 1 nm), while severely activated carbon (KOH/hydrochar ratio of 2) has broad micropores and narrow mesopores between 2 and 3 nm. This multimodel porous structure can form a network with different cavities, which is beneficial for both supercapacitors and CO_2 capture.

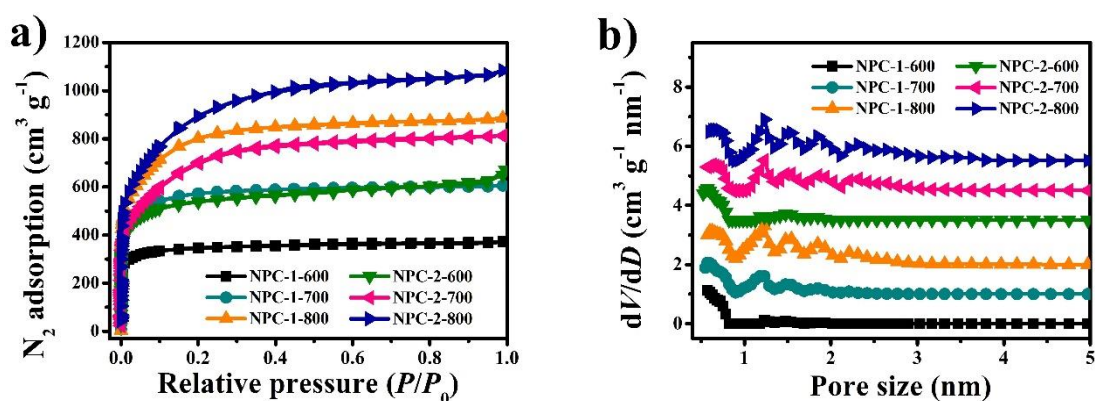


Figure 4. Nitrogen sorption isotherms (a) and pore size distribution curves (b) of nitrogen-doped porous carbon

The textural parameters of the nitrogen-doped porous carbon are listed in Table 1. As the activation temperature or mass ratio of KOH/hydrochar increases, the BET surface area and pore volume increase from 1340 to 3273 $m^2 g^{-1}$ and from 0.58 to 1.68 $cm^3 g^{-1}$, respectively. Importantly, the micropores contribute greatly to the surface area and pore volume, favoring both the supercapacitance and CO_2 uptake. Furthermore, the severely activated carbon materials possess high porosity with abundant mesopores. This hierarchical porous structure not only offers a large surface area for charge accommodation and CO_2 storage but also facilitates ion and gas transfer in the pores.

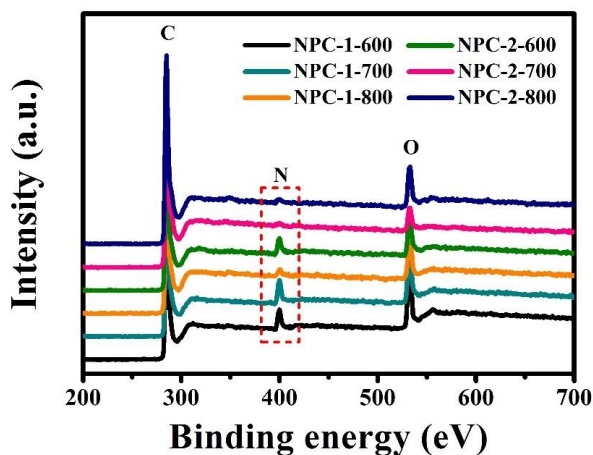
To identify the surface chemical properties of NPC materials, elemental analysis and XPS were performed. We can see from Table 1 that hydrochar has a high nitrogen content of 14.59 wt%, while the nitrogen content gradually decreases when the hydrochar is activated with KOH. The nitrogen content decreases from 7.03 wt% in the sample subjected to the mildest activation (NPC-1-600) to 1.34 wt% of the sample most severely activated sample (NPC-2-800), suggesting the instability of nitrogen groups in the chemical activation processes.

Table 1. Textural properties of the nitrogen-doped porous carbon

Samples	Textural properties						
	S_{BET} ($\text{m}^2 \text{g}^{-1}$) ^a	V_{t} ($\text{cm}^3 \text{g}^{-1}$) ^b	$I_{\text{D}}/I_{\text{G}}$	Nitrogen content (wt%)	CO_2 uptake (mmol g^{-1}) ^c	Capacitance (F g^{-1}) ^d	Equivalent series resistance
Hydrochar	—	—	—	14.59	—	—	—
NPC-1-600	1340(1305)	0.58(0.54)	1.02	7.03	4.4(6.7)	271	0.068 Ω
NPC-1-700	2173(2128)	0.94(0.89)	1.03	3.31	3.9(6.1)	279	0.119 Ω
NPC-1-800	3018(2898)	1.37(1.25)	1.05	1.96	3.5(5.9)	307	0.078 Ω
NPC-2-600	2072(1813)	1.04(0.72)	1.05	6.41	3.9(6.2)	282	0.116 Ω
NPC-2-700	2530(2399)	1.26(1.21)	1.10	2.73	3.5(5.7)	296	0.095 Ω
NPC-2-800	3273(3019)	1.68(1.41)	1.14	1.34	3.6(5.7)	333	0.082 Ω

^aValues in parentheses are micropore areas. ^bValues in parentheses are micropore volumes. ^cValues are measured at 25 °C, and the values in parentheses are measured at 0 °C. ^dValues are measured at a current density of 0.5 A g^{-1} .

Furthermore, the XPS survey spectra (Figure 5) indicate that these carbon materials only contain N, C and O elements, implying the high purity of the as-synthesized carbon materials. Additionally, the element mapping images of NPC-1-600 (Figure 6) indicate the uniform distribution of N, C and O elements in the carbon frameworks. The N 1s spectra of all carbon materials are shown in Figure 7. They can be deconvoluted into three peaks, representing pyridinic nitrogen (N-6 at ~398.6 eV), pyridine nitrogen (N-5, ~400.2 eV), and quaternary nitrogen (N-Q at ~401.3 eV) [24-26]. These results demonstrate the successful introduction of nitrogen species into carbon frameworks, which benefits the enhanced performance of both supercapacitors and CO_2 capture.

**Figure 5.** XPS survey spectra of NPC

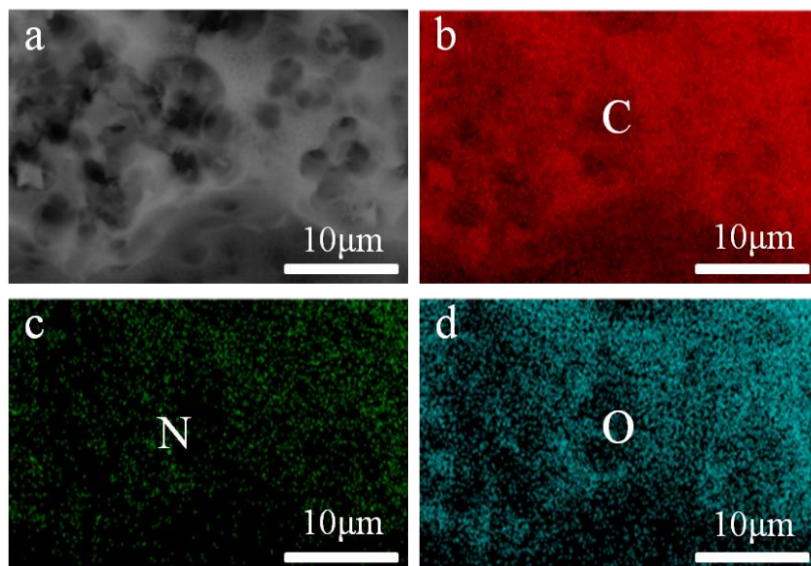


Figure 6. Elemental mapping of NPC-1-600

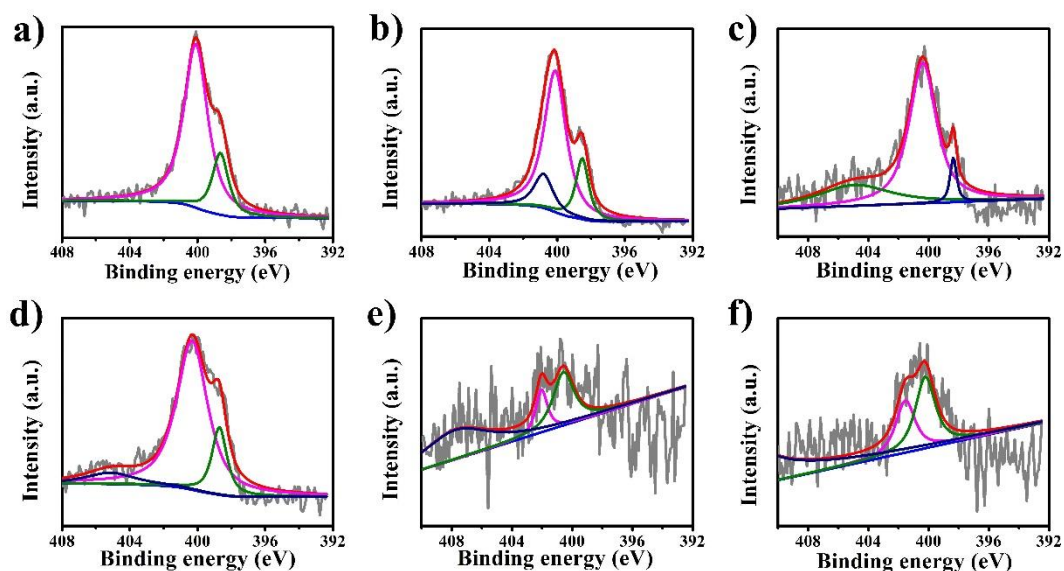


Figure 7. N 1s XPS spectra of NPC-1-600 (a), NPC-1-700 (b), NPC-1-800 (c), NPC-2-600 (d), NPC-2-700 (e), and NPC-2-800 (f)

NPC materials with well-developed porosity and high nitrogen content are also employed as supercapacitor electrodes. The capacitive performance of the carbon materials is investigated using CV, GCD and EIS measurements operated in 6.0 M KOH. The comparative CV curves of all the NPC electrodes conducted at a scanning rate of 10 mV s^{-1} exhibit a nearly rectangular shape (Figure 8(a)), indicating the typical electrical double-layer capacitance behavior. Moreover, wide humps are observed in the range from -0.7 to -0.3 V, presumably due to redox reactions caused by nitrogen species [27,28]. It is noteworthy that NPC-2-800 shows a larger CV area than the other carbon materials, suggesting the highest specific capacitance. This is because the specific capacitance is directly proportional to the

integrated CV curves. The GCD curves of all samples (Figure 8(b)) measured at a current density of 0.5 A g⁻¹ exhibit an asymmetric situation owing to the presence of pseudocapacitances provided by nitrogen species and ion transport limitation in the micropores. The specific capacitances of all samples are listed in Table 1, which are calculated from Equation (1). As expected, the discharge time of the NPC-2-800 electrode is longer than that of the other electrodes, suggesting the largest specific capacitance of the NPC-2-800 electrode. NPC-2-800 exhibits a high specific capacitance of 333 F g⁻¹ at 0.5 A g⁻¹ due to the presence of well-developed micro/mesopores and nitrogen content. Interestingly, the specific capacitance is not in direct proportion to the surface area because not all pores contribute to charge accumulation, and nitrogen functional groups can also generate pseudo capacitance. Additionally, the rate performance is a significant factor for the rapid charging and delivery of energy. The specific capacitances of carbon materials measured at different current densities are displayed in Figure 8(c). Importantly, the capacitance retention of all samples is over 70% as the current density increases to 10 A g⁻¹, implying good rate performance. The NPC-2-800 electrode has specific capacitances of 333, 312, 285, 268, and 259 F g⁻¹ at current densities of 0.5, 1, 2, 5, and 10 A g⁻¹, respectively, which are superior to many reported carbon materials in the literature (Table 2). Furthermore, the cycle stability of all electrodes was measured at 10 A g⁻¹ (Figure 9). Each NPC electrode exhibited a slight decrease in the specific capacitance after 5000 charge/discharge cycles, maintaining good capacitance retentions of 89.8, 91.3, 92.9, 89.7, 91.8, and 92.7%, demonstrating the outstanding long-term durability of these electrodes.

Table 2. Summary of electrochemical performance of different carbon electrodes

Samples	C (F g ⁻¹) ^a	R (A g ⁻¹) ^b	El ^c	References
Nitrogen-doped porous carbon	333	1	6 M KOH	[29]
Nitrogen-doped asphaltene-based porous carbon fibers	301	1	6 M KOH	[30]
Nitrogen-doped porous carbon balls	341	1	6 M KOH	[10]
Carbon from pyrene-based CMP	301	1	6 M KOH	[31]
Nitrogen-doped porous carbon	334	1	6 M KOH	[32]
Nitrogen-doped hierarchically porous carbon nanosheets	203	0.5	6 M KOH	[33]
Nitrogen-doped porous carbon	340.2	0.5	6 M KOH	[34]
Hierarchical porous carbon	283	1.0	6 M KOH	[35]
Nitrogen-doped porous carbon	333	0.5	6 M KOH	This work

^aSpecific capacitance.

^bCurrent density.

^cElectrolyte.

Figure 8(d) exhibits electrochemical impedance spectra, offering the frequency response of nitrogen-doped porous carbon in EDLCs. In the high-frequency region, the Nyquist plots represent a semicircle of all samples (see the inset of Figure 8(d)), which is relative to the interfacial resistance caused by charge transfer at the electrode/electrolyte interface [36,37]. The equivalent series resistance (ESR) of the NPC sample is listed in Table 1. The ESR of NPC-1-600 is 0.068Ω , which is the smallest. The largest ESR was observed for NPC-1-700 (0.119Ω). All NPC samples exhibit a small value, which implies that the carbon materials have low interface contact resistance because they have a suitable pore size distribution and nitrogen species that are favorable for electrolyte ion transport. In the low frequency region, the slope of lines denotes an ideal capacitive behavior owing to the diffusion of the electrolyte ions in the pores of electrodes [35,38]. Obviously, NPC-2-800 exhibits the largest slope, which reveals that the NPC-2-800 possesses the best conductivity among the synthesized nitrogen-doped porous carbons. The Warburg resistance for the electrolyte ions can cause a shift in the vertical line [37]. The NPC-2-800 electrode exhibits the lowest Warburg resistance. These results demonstrate that the nitrogen-doped porous carbon, especially NPC-2-800, possesses high electrical conductivity, which is beneficial for supercapacitors.

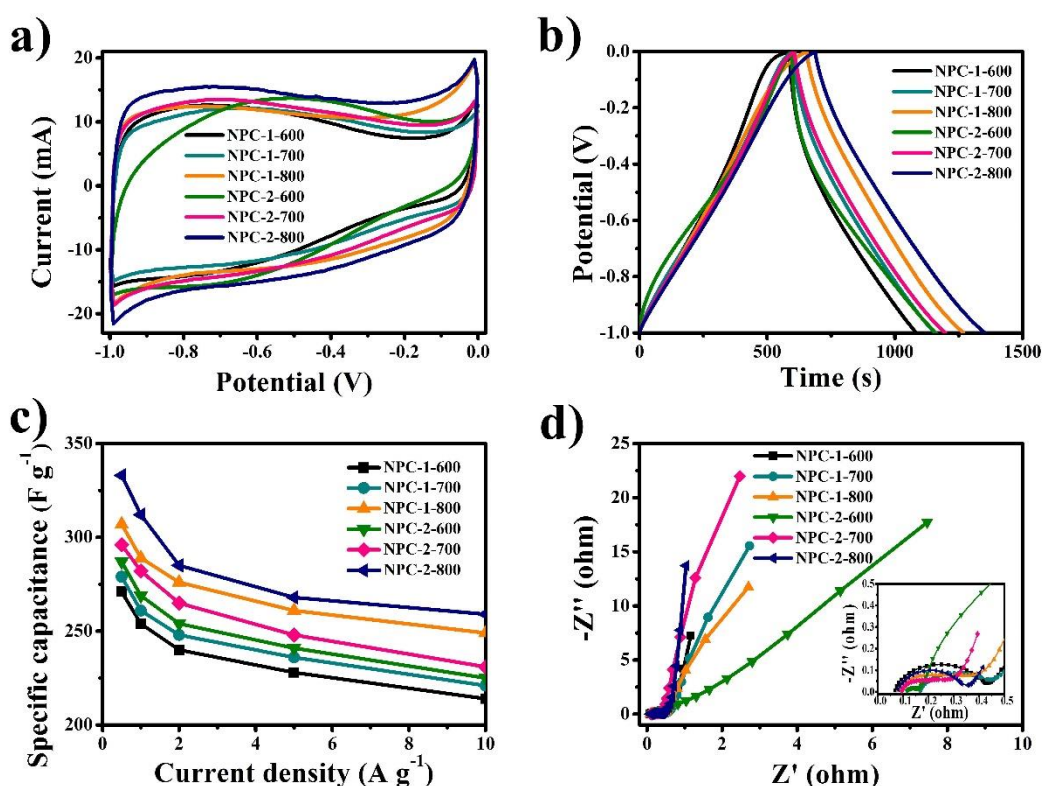


Figure 8. CV curves at a scan rate of 10 mV s^{-1} (a), charge–discharge curves at a current density of 0.5 A g^{-1} (b), rate capability at current densities of $0.5, 1, 2, 5,$ and 10 A g^{-1} (c), and Nyquist plots (d) for the synthesized carbon materials

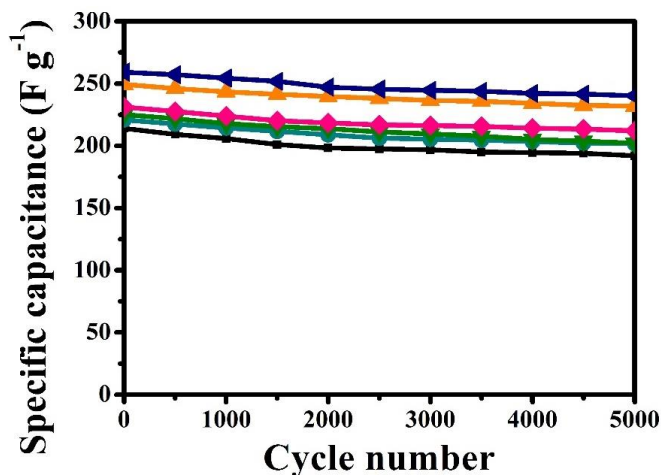


Figure 9. Cycle life measurement at a current density of 10 A g^{-1} for the synthesized carbon materials

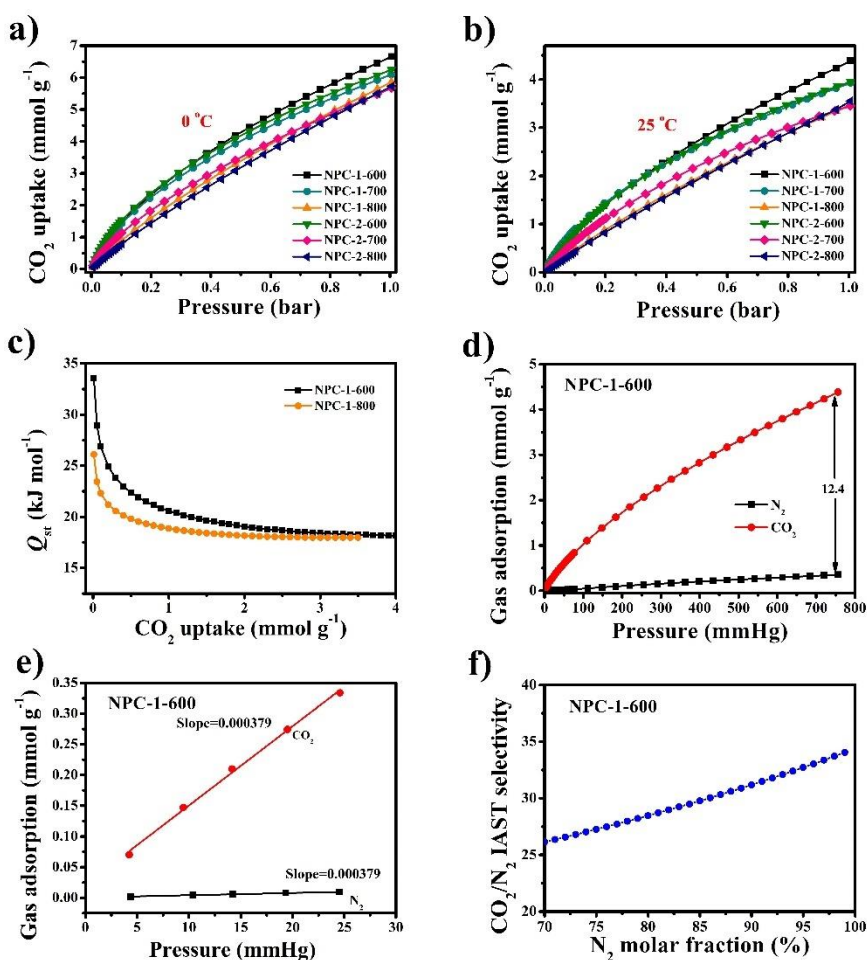


Figure 10. Carbon dioxide adsorption isotherms of nitrogen-doped porous carbon at $0 \text{ }^\circ\text{C}$ (a) and $25 \text{ }^\circ\text{C}$ (b); isosteric heat of CO_2 adsorption calculated from CO_2 uptakes of NPC-1-600 and NPC-1-800 (c); CO_2 and N_2 adsorption isotherms of NPC-1-600 (d) and initial slope (e) calculated from CO_2 and N_2 adsorption isotherms at $25 \text{ }^\circ\text{C}$; CO_2/N_2 selectivity versus N_2 molar fraction with an overall pressure of 1 bar for NPC-1-600 at $25 \text{ }^\circ\text{C}$ (f). The calculation was based on single-component gas adsorption data by the IAST method.

On the other hand, the as-synthesized nitrogen-doped porous carbon has promising potential for CO₂ capture. The CO₂ adsorption isotherms collected at 1 bar are shown in Figure 10(a) and Figure 10(b), and the capacity of CO₂ adsorption is summarized in Table 1. The carbon materials have high CO₂ uptake in the range of 5.7-6.7 and 3.5-4.4 mmol g⁻¹ at 0 and 25 °C, respectively, indicating high CO₂ capture performance. Note that the carbon materials prepared with KOH/hydrochar = 1 show noticeably higher CO₂ uptake than those prepared with KOH/hydrochar = 2, despite the severely activated carbon materials possessing more porous structures.

This is because the mildly activated carbon materials possess a narrower pore size distribution and higher nitrogen content than those prepared with severe activation. Indeed, several investigations have demonstrated that ultramicropores are more efficient for CO₂ uptake than large pores because of their stronger interaction between carbon and CO₂ molecules. The adsorption energy for CO₂ capture is optimized when the pore size is two times (in the case of slit-shaped pores) or three times (in the case of cylindrical-shaped pores) that of the CO₂ molecule [39]. The kinetic diameter of the CO₂ molecule is 0.33 nm, so the optimal pore size is between 0.7 and 0.9 nm, which can illustrate the excellent CO₂ capture performance of carbon materials prepared with mild activation, since the porosity of these carbon materials is mainly dominated by ultramicropores between 0.6 and 0.9 nm. On the other hand, the incorporation of nitrogen species into carbon lattices greatly changes the electronic structure of carbon layers, resulting in a strong interaction between carbon and CO₂ molecules, which is derived from the pole-pole interactions between the large quadrupole moment of CO₂ molecules (13.4×10^{-40} C m²) and the polar sites associated with nitrogen groups [40,41]. The strong interaction between carbon materials and CO₂ molecules can be assessed by the isosteric heat of adsorption (Q_{st}) calculated from the Clausius–Clapeyron equation using adsorption data collected at 0 and 25 °C (see supporting information). The isosteric heat of CO₂ adsorption is shown in Figure 10(c). As the CO₂ adsorption capacity increases from 0.1 to 4.0 mmol g⁻¹, the Q_{st} of sample NPC-1-600 decreases from 33.6 to 18.1 kJ mol⁻¹, and the Q_{st} of sample NPC-1-800 decreases from 26.1 to 18.0 kJ mol⁻¹, gradually remaining constant. These results indicate that NPC-1-600 has higher CO₂ uptake than NPC-1-800 because NPC-1-600 shows a larger interaction with CO₂ molecules than NPC-1-800. Thus, it is highly desirable to design and prepare carbon materials with abundant narrow microporosity and nitrogen functional groups.

For practical applications, sorbents require high CO₂/N₂ selectivity for postcombustion CO₂ capture since typical flue gas streams mainly contain CO₂ (~15%) and N₂ (~85%). To estimate the selectivity for the separation of CO₂ from N₂, the CO₂ and N₂ adsorption isotherms were measured at room temperature. As shown in Figure 10(d), the CO₂ uptake of NPC-1-600 (4.4 mmol g⁻¹) is drastically larger than the N₂ uptake (0.4 mmol g⁻¹), and the selectivity for CO₂ over N₂ is estimated to be 34:1 based on the ratio of the initial slopes of the CO₂ and N₂ adsorption isotherms (Figure 10(e)), suggesting that sample NPC-1-600 has high performance for the separation of CO₂ from N₂, which is suitable for industrial applications. Furthermore, the ideal adsorbed solution theory (IAST) model was further employed to assess the selectivity of CO₂ over N₂ for NPC-1-600 (see supporting information). As shown in Figure 10(f), the selectivity of CO₂ against N₂ is calculated in the range between 26 and 46 at 70-100% CO₂ concentration, which corresponds with the result of the initial slope method. Impressively, an IAST selectivity factor of 30 is obtained at a total pressure of 1 bar with a 15% CO₂ concentration, suggesting superior CO₂ uptake from a flue gas stream.

4. CONCLUSION

Highly porous nitrogen-doped carbon materials were synthesized via hydrothermal carbonization and KOH activation using sustainable adenine and glucose as nitrogen and carbon sources, respectively. The as-synthesized carbon materials have the characteristics of a high surface area, large pore volume, and high nitrogen content. As a result, a high specific capacitance of 333 F g⁻¹ is achieved in 6 M KOH at a current density of 0.5 A g⁻¹ with excellent rate capability and long cycle life (>90% capacity retention after 5000 cycles). Moreover, a large CO₂ uptake of 4.4 mmol g⁻¹ at 25 °C is obtained with excellent performance for CO₂/N₂ separation with high CO₂/N₂ selectivity up to 34 and 30 (calculated by the initial slope method and IAST, respectively). This work demonstrates the importance of high porosity and nitrogen doping on improving the performance in supercapacitors and CO₂ capture.

ACKNOWLEDGEMENTS

Authors acknowledged the financial support of Qingdao University of Science and Technology towards the open access of this research work.

References

1. H. Yu, W. Wang, F. Lin, K. Li, B. Yan, Y. Song, C. Huang and G. Chen, *Sep. Purif. Technol.*, 276(2021)119291.
2. X.-y. Luo, Y. Chen and Y. Mo, *New Carbon Mater.*, 36(2021)49.
3. S. Ott, A. Orfanidi, H. Schmies, B. Anke, H. N. Nong, J. Hübner, U. Gernert, M. Glied, M. Lerch and P. Strasser, *Nat. Mater.*, 19(2020)77.
4. B. Yao, H. Peng, H. Zhang, J. Kang, C. Zhu, G. Delgado, D. Byrne, S. Faulkner, M. Freyman, X. Lu, M. A. Worsley, J. Q. Lu and Y. Li, *Nano Lett.*, 21(2021)3731.
5. J. Miao, W. Geng, P. J. J. Alvarez and M. Long, *Environ. Sci. Technol.*, 54(2020)8473.
6. L. Jiang, Y. Zhang, M. Zhou, L. Liang and K. Li, *J. Hazard. Mater.*, 358(2018)53.
7. D. Wang, Z. Wang, Y. Li, K. Dong, J. Shao, S. Luo, Y. Liu and X. Qi, *Appl. Surf. Sci.*, 464(2019)422.
8. C. Wang, H. Wang, B. Dang, Z. Wang, X. Shen, C. Li and Q. Sun, *Renew. Energy*, 156(2020)370.
9. L. Guan, L. Pan, T. Peng, C. Gao, W. Zhao, Z. Yang, H. Hu and M. Wu, *ACS Sustain. Chem. Eng.*, 7(2019)8405.
10. R. Vinodh, R. S. Babu, C. V. V. M. Gopi, C. Deviprasath, R. Atchudan, L. M. Samyn, A. L. F. de Barros, H.-J. Kim and M. Yi, *J. Energy Storage*, 28(2020)101196.
11. F. Meng, Z. Gong, Z. Wang, P. Fang and X. Li, *Fuel*, 251(2019)562.
12. Z. Zhang, B. Wang, C. Zhu, P. Gao, Z. Tang, N. Sun, W. Wei and Y. Sun, *J. Mater. Chem. A*, 3(2015)23990.
13. E. Qezelsefloo, S. Khalili, M. Jahanshahi and M. Peyravi, *Mater. Chem. Phys.*, 239(2020)122304.
14. S. S. Sekhon, P. Kaur and J.-S. Park, *Renew. Sust. Energ. Rev.*, 147(2021)111173.
15. J. Ou, Y. Zhang, L. Chen, Q. Zhao, Y. Meng, Y. Guo and D. Xiao, *J. Mater. Chem. A*, 3(2015)6534.
16. X. Mao, Z. Cao, S. Chen, J. Jia, X. Li, Y. Yin and S. Yang, *Int. J. Hydrogen Energy*, 44(2019)5890.
17. L. Xu, L. Ma, X. Zhou, Y. Ling, X. Wang and M. Chen, *Appl. Surf. Sci.*, 458(2018)86.
18. I.-A. Choi, D.-H. Kwak, S.-B. Han and K.-W. Park, *J Ind. Eng. Chem.*, 63(2018)112.
19. T. V. Tran, D. T. C. Nguyen, H. T. N. Le, D.-V. N. Vo, V.-D. Doan, V.-P. Dinh, H.-T. T. Nguyen, T. D. Nguyen and L. G. Bach, *C. R. Chim.*, 22(2019)804.
20. D. Q. Dao, T. K. Anh Nguyen, S. G. Kang and E. W. Shin, *ACS Sustain. Chem. Eng.*, 9(2021)14537.

21. Y. Park, K. P. S. S. Hembram, R. Yoo, B. Jang, W. Lee, S.-G. Lee, J.-G. Kim, Y.-I. Kim, D. J. Moon, J.-K. Lee and J.-K. Lee, *J. Phys. Chem. C*, 123(2019)14003.
22. F. Rosenburg, E. Ionescu, N. Nicoloso and R. Riedel, *Materials*, 11(2018)93.
23. H. Teng and L.-Y. Hsu, *Ind. Eng. Chem. Res.*, 38(1999)2947.
24. J. R. Pels, F. Kapteijn, J. A. Moulijn, Q. Zhu and K. M. Thomas, *Carbon*, 33(1995)1641.
25. S. Biniak, G. Szymański, J. Siedlewski and A. Świątkowski, *Carbon*, 35(1997)1799.
26. J. Lahaye, G. Nansé, A. Bagreev and V. Strelko, *Carbon*, 37(1999)585.
27. Y. Yang, Y.-x. Liu, Y. Li, B.-w. Deng, B. Yin and M.-b. Yang, *J. Mater. Chem. A*, 8(2020)17257.
28. S. Zhang, Y. Zhang, G. Shao and P. Zhang, *Nano Res.*, 14(2021)3942.
29. H. Pan, Y. Zhang, Y. Pan, W. Lin, W. Tu, H. Zhang, *Chem. Eng. J.*, 401(2020)126083.
30. G. Ni, F. Qin, Z. Guo, J. Wang, W. Shen, *Electrochim. Acta*, 330(2020)135270.
31. Y. Zhao, F. Xie, C. Zhang, R. Kong, S. Feng, J.-X. Jiang, *Micropor. Mesopor. Mater.*, 240(2017)73.
32. M. Wu, S. Tong, L. Jiang, B. Hou, X. Li, Y. Zhang, J. Yue, M. Jiang, L. Sheng, *J. Alloy. Compd.*, 844(2020)156217.
33. M. Wang, J. Yang, S. Liu, M. Li, C. Hu, J. Qiu, *J. Colloid Interf. Sci.*, 560(2020)69.
34. Z. Chen, M. Zhang, Y. Wang, Z. Yang, D. Hu, Y. Tang, K. Yan, *Green Energy Environ.*, 6(2021)929.
35. D. Zhu, Y. Wang, W. Lu, H. Zhang, Z. Song, D. Luo, L. Gan, M. Liu and D. Sun, *Carbon*, 111(2017)667.
36. V. S. Sumana, Y. N. Sudhakar, V. Anitha and G. K. Nagaraja, *Electrochim. Acta*, 353(2020)136558.
37. P. Veerakumar, A. Sangili, S. Manavalan, P. Thanasekaran and K.-C. Lin, *Ind. Eng. Chem. Res.*, 59(2020)6347.
38. G. Ma, Q. Yang, K. Sun, H. Peng, F. Ran, X. Zhao and Z. Lei, *Bioresour. Technol.*, 197(2015)137.
39. A. Rehman and S.-J. Park, *J. CO₂ Util.*, 34(2019)656.
40. F. Qin, Z. Guo, J. Wang, S. Qu, P. Zuo and W. Shen, *Appl. Surf. Sci.*, 491(2019)607.
41. D. Britt, H. Furukawa, B. Wang, T. G. Glover and O. M. Yaghi, *P. Natl. Acad. Sci. USA*, 106(2009)20637.